12

Multidimensional Design of Hydraulic Components and Systems

Massimo Milani, Luca Montorsi and Fabrizio Paltrinieri
DISMI – University of Modena and Reggio Emilia
Italy

1. Introduction

The importance of numerical simulation in hydraulic components design is rapidly increasing. In fact, the computational simulations of compressible and incompressible flows can relevantly support experiments, and the CFD is becoming a valuable tool also for the design and the pre-prototyping processes (Yang, 2002, 2005; Barman, 2005). Moreover, the human and computational resources to be involved in the numerical analysis are now not only acceptable, but also advantageous, thanks to the continuous development of computational platforms, as well as of the CFD tools.
Nevertheless the accuracy and reliability of the numerical results must be addressed when approaching a new problem, since they demonstrated to be very sensitive to the fluid-dynamics characteristics of the case studied (such as the Reynolds number in the critical sections, the geometry complexity and the boundary conditions). For example, the widely used cylindrical orifices (metering valves, directional valves, injectors, instruments, etc.) show that the fluid dynamic performance is significantly affected by the geometrical details; consequently, a sharp-edge inlet presents an efflux coefficient lower than a rounded one (Ohrn et al., 1991), while small modifications in the curvature can determine remarkable differences both in the flow field, and in pressure losses.
Furthermore, a key feature in the design process of fluid power components and systems is the capability of controlling or avoiding cavitation and aeration. The problems caused by the cavitating phenomena are widely known (Oshima & Ichikawa, 1985, 1986) and they can lead to efficiency loss, vibrations and noise, unexpected change in the characteristics of flow rate and flow forces and even erosion of the components when the phenomenon becomes particularly aggressive (Oshima e al., 2001).
Therefore, the possibility of predicting cavitation is fundamental in hydraulic components design and both experiments and numerical simulation have to be employed and integrated in order to help the understanding of the basics of cavitation occurrence. Particularly, numerical analysis can provide a great amount of data that can extend the experimental area and deepen the insight of the physical phenomenon (Yang, 2002, 2005). Nevertheless, the accuracy and reliability of the numerical models have to be addressed when approaching a new problem or when they are modified to account for a more detailed description of the physical process. The model sensitivity with respect to the fluid-dynamics characteristics of the case studied (such as the Reynolds number in the critical sections, the geometry

complexity and the boundary conditions) must be properly addressed before adopting the numerical tool as a predictive design tool.
When addressing numerically the flow through the metering section of hydraulic components, particular care should also be devoted to the operating conditions accounted for in the simulations. In fact, the behaviour of the flow is usually highly time dependent, as well as the geometry of the component varies according to the working conditions. Thus, the choice of carrying out a steady state or a fully transient CFD simulation of the component is a critical issue in the design methodology. On one hand, the former approach is characterized by a significantly lower computational effort as well as a shorter case setup time, but it evaluates the fluid-dynamics performance of the hydraulic component only under the assumption of steady state operation, which is often a very limiting restriction compared to the real operations. Conversely, the fully transient CFD calculation predicts more accurately the real behaviour of the flow within the hydraulic component, but the required computational effort is remarkably large and both the setup time and the simulation execution duration can be considerably long. Therefore, it is important to highlight the quality of the results that can be obtained by performing these two types of CDF simulations, in order to select the correct approach for each analysis that has to be carried out.
In this chapter, the above mentioned critical aspects in the application of multidimensional numerical analysis for the design of mechanical devices and components for hydraulic systems are addressed. The objective of the chapter is to provide a roadmap for the multidimensional numerical analysis of the hydraulic components to be used effectively in the design process. In particular, two examples of hydraulic systems are accounted for in the application of the CFD analysis: a proportional control valve and a fuel accumulator for multi-fuel injection systems. These test cases have been selected due to their representativeness in the field of hydraulic applications and to the complexity and variety of the physical phenomena involved.

2. Prediction capabilities of the numerical models

The Navier–Stokes equations for isothermal, incompressible flows are solved by means both of the open source multidimensional CFD code OpenFOAM (OpenCFD, 2010, OpenFOAM®-Extend Project, 2010), and the commercial CFD code ANSYS CFX. Bounded central differencing is used for the discretization of the momentum, second-order upwind for subgrid kinetic energy. Pressure–velocity coupling was achieved via a SIMPLE similar procedure. The second-order implicit method is used for time integration scheme. No time integration scheme is involved, and all the calculations are performed under steady state conditions.
In the modeling of the turbulent cases the performance of three turbulence models are investigated:

1. The standard k-ε model (KE), including wall functions for the near-wall treatment;
2. the a low-Reynolds number model developed by Launder and Sharma (LS), (Launder & Sharma, 1974) in which the transport equations for the turbulent quantities are integrated to the walls;
3. the two zonal version of the k-ω model, known as the shear stress transport model (SST) (Menter, 1993).

Since the objective of this investigation is the analysis of confined flows, the attention is paid to near-wall behaviour, to the damping functions and to the boundary conditions. Hence the choice of addressing the predictive capabilities of turbulence models with a different near wall treatment is made. In the k-ε model, the transport equations are not integrated to the walls. Instead the production and dissipation of kinetic energy are specified in the near-wall cell, using the logarithmic law-of-the-wall. The validity of the near wall treatment requires that the values of the y^+ must be in the range between 30 and 100. In the k- ε model formulation proposed by Launder and Sharma the definition of the turbulent kinetic energy dissipation is modified to account for the low Reynolds regions close to the wall. In fact, this equation is solved for $\tilde{\varepsilon}$ instead of ε, and a new term E is added to compensate for additional production and to further balance diffusion and dissipation in the vicinity of the walls. In this way, the Launder and Sharma approach has the advantage of the natural boundary condition $\tilde{\varepsilon} = 0$ at the walls. The model's constants are the same as the standard formulation, but the damping factor functions are evaluated as a function of the turbulent Reynolds number. The boundary conditions at the wall are $k_\omega = 0$ and $\tilde{\varepsilon} = 0$. For the low Reynolds number turbulence models the requirement on the y^+ values is more stringent, in fact y^+ should never be larger than one. The. shear stress transport model is derived from the original two zonal version of the k-ω model proposed by Wilcox (Wilcox, 1988), and based on the transport equation proposed by Kolmogorov. In this model the damping functions in near-wall regions are not necessary. The eddy viscosity is calculated as the ratio between the turbulent kinetic energy and the the specific dissipation, ω. The original version of the model demonstrated to be very sensitive to ω specified in the free-stream (Menter, 1994). Therefore a new formulation was proposed by Menter combining the the k- ω model by Wilcox in the inner region of the boundary layer, and the standard k - ε in the outer region and the free-stream. The ω equation differs from the one of the original k-ω model because of an additional cross-diffusion term. In the inner part of the boundary region the model's constants are the same as the k-ω model, while in the outer region they become similar the k–ε ones. The boundary conditions do not change from the original k-ω model formulation, and similarly require y^+ smaller than 3. In this analysis careful attention was paid in order to comply with the requirements on the y^+ values for the different turbulence models adopted.

2.1 Flow through a circular pipe

First phase of the analysis is the simulation of the fundamental test case represented by the flow through a circular pipe. The geometrical domain is assumed to be a straight circular pipe, characterized by an axial length equal to 1.0 m and a diameter of 10 mm, pure water is considered as the operating fluid and both laminar and turbulent conditions are accounted for. Due to the axial symmetry of both the geometry and the boundary conditions, the simulations assume a two dimensional domain. Therefore, the meshes are defined as circular sectors with an angular amplitude equal to 5° (see Fig.1).

A preliminary sensitivity analysis with respect to the grid resolution is carried out, in order to assess the best compromise between the accuracy of the results and the computational cost. Different grids are constructed varying the cell spacing both in the axial and radial direction. For the laminar case, the cell axial dimensions equal to 1.0, 2.5, and 10 mm are compared keeping constant the resolution along the cylinder radius (i.e. 0.3 mm); whereas the grids used in the turbulent case are characterized by a radial cell size equal to 0.3, 0.1

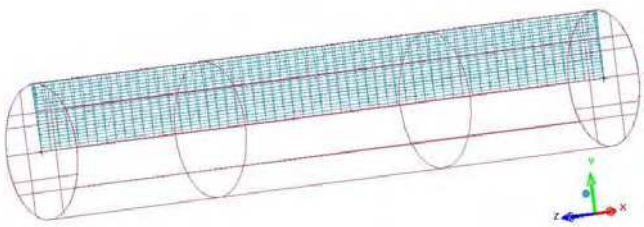

Fig. 1. 2D mesh for the straight circular pipe

Case #	CFD code	Grid (ax. & rad.)	Turbulence Model
A_1; A_2; A_3; A_4	FOAM	1.0x0.3; 2.5x0.3; 5.0x0.3; 10.0x0.3	Laminar
A_5; A_6; A_7; A_8	CFX	1.0x0.3; 2.5x0.3; 5.0x0.3; 10.0x0.3	Laminar
A_9; A_10; A_11	FOAM	5.0x0.05; 5.0x0.1; 5.0x0.3	LS
A_12; A_14; A_16	CFX	5.0x0.05; 5.0x0.1; 5.0x0.3	KE
A_13; A_15; A_17	CFX	5.0x0.05; 5.0x0.1; 5.0x0.3	SST

Table 1. List of simulations for the laminar and turbulent flow through the circular pipe

and 0.05 mm and a constant axial dimension (i.e. 5 mm). The meshes consist only in hexahedrons and prisms along the cylinder axis; the height of the cells near the walls is carefully chosen in order to comply with the requirements of the turbulence models used in the simulations on the distance to the wall of the first node. Table 1 shows the comprehensive list of the simulations performed. For the laminar cases a fluid axial velocity of 0.1 m/s is set at the inlet boundary, while a static pressure boundary condition was considered at the pipe outlet. The numerical results for the laminar regime were compared with the Hagen-Poiseuille theory (Pao, 1995), that is applicable when no relative motion between the fluid and the wall appears, and an incompressible Newtonian fluid undergoes to a isothermal laminar flow. Under these assumptions, the axial velocity profile versus the distance from the axis can be determined from the expression:

$$v = \frac{1}{4\mu} \cdot \left(-\frac{\partial p}{\partial z} \right) \cdot \left(r_0^2 - r^2 \right) \tag{1}$$

As well known, the laminar velocity assumes the fully developed profile at a distance from the pipe inlet on the basis of the Langhaar length, defined as:

$$L' = 0.058 \cdot \mathrm{Re} \cdot D \tag{2}$$

In Figs. 2 a) and c) the theoretical axial velocity profile as a function of the distance from the cylinder axis is compared with the calculated profiles for the different grid resolutions. Both codes used in the simulations demonstrated a good agreement with the axial velocity profile derived from the Hagen-Poiseuille, and also demonstrated a negligible influence on the cell dimension. Similar behaviour could be noticed in the velocity profile prediction, see Figs. 2 b) and d), and practically no differences could be seen among the simulated cases.
When investigating the flow field under fully turbulent conditions a fluid axial velocity of 5.0 m/s was set at the inlet boundary. Calculations were performed for three grids having

different cell dimensions, and the performance of the turbulence models described in the previous sections (i.e. the standard k - ε model, the k – ω shear stress transport model and the low Reynolds Launder-Sharma models) is investigated. The results were compared with the experimental measurements performed by Nikuradse available in literature (Pao, 1995). In Figs. from 3 to 5 the axial velocity versus the distance from the cylinder axis and the cylinder outlet are depicted. The KE model demonstrated a good agreement with the measurements and a scarce sensitivity to the grid size; in particular the logarithmic law-of-the-wall was able to capture the curvature of the axial velocity in proximity to the wall. Whereas, the SST model resulted to be remarkably more influenced by the mesh resolution. In fact Fig. 4 b) shows that the predicted axial velocity differs significantly for the three simulated grids. In particular the coarser grid calculation underestimates the velocity magnitude, while the discrepancy between the curves relating the fine and intermediate meshes are less evident and closer to the results found for the KE model. The more evident sensitivity of the SST model to the grid size is due to the stricter requirement on the distance of the first grid node to the wall. The sensitivity to the mesh resolution was found to be even more marked for the LS model (see Fig. 5). In this model, in fact, the transport equations are integrated up to the wall and the effect of the near wall cell is more directly transferred to the inner domain. This model demonstrated to overestimate the axial velocity in the core region as a consequence of the velocity magnitude tendency when approaching the wall boundary. The dissipation of the turbulent kinetic energy is therefore overestimated and the model constant should be tuned accordingly. For the present study the constants of the considered models were kept the same as the suggested values.

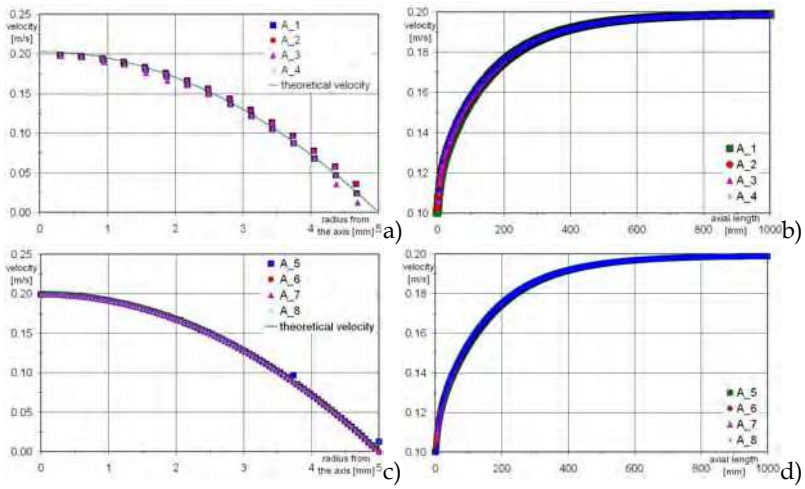

Fig. 2. a) and c) Axial velocity profile vs. the distance from the axis and b) and d) axial velocity profile along the cylinder axis vs. the distance from the pipe inlet: comparison among different grid resolutions (laminar regime)

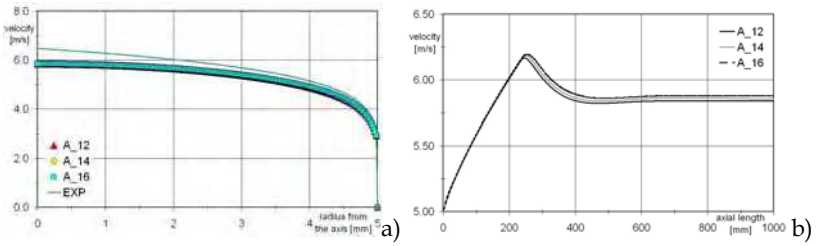

Fig. 3. a) Axial velocity profile vs. the distance from the axis and b) Axial velocity profile along the cylinder axis vs. the distance from the pipe inlet: comparison among different grid resolutions (KE model)

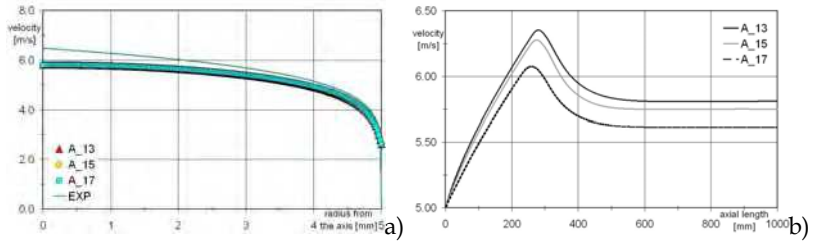

Fig. 4. a) Axial velocity profile vs. the distance from the axis and b) Axial velocity profile along the cylinder axis vs. the distance from the pipe inlet: comparison among different grid resolutions (SST model)

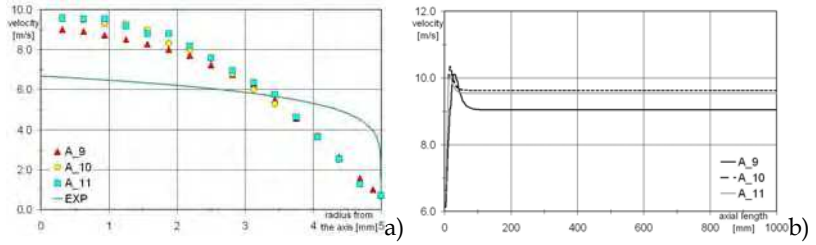

Fig. 5. a) Axial velocity profile vs. the distance from the axis and b) Axial velocity profile along the cylinder axis vs. the distance from the pipe inlet: comparison among different grid resolutions (LS model)

2.2 Flow through a small sharp-edged cylindrical orifice

Further step of the analysis is the investigation of the flow pattern through a sharp-edged cylindrical orifice. Although the geometry of this test case is very simple, it well represents the fluid-dynamics conditions which can be found in the critical sections of many hydraulic components. In addition, experimental measurements of the flow through abrupt section change in circular pipes are available in literature. Therefore, it is possible to address the predictive capabilities of the numerical calculations by comparing the main flow

characteristics with experiments. In the present work the measurements carried out by Ramamurthi and Nandakumar in 1999 were taken as a reference. In the experiments, with reference to pure water, the effects of varying the diameters of the sharp-edge orifice and the ratio of the inlet diameter (d) and the orifice length (l) are investigated for different Reynolds numbers of operation. The experimental set-up consisted of a tank for the water, a nitrogen gas source for pressurizing the tank and a feed-line fitted with flow control valves for supplying water to the orifice. The modelling of the experimental device focuses only on the orifice geometry, and particular care is paid to assure that the flow at the orifice extremes is not influenced by the inlet and outlet of the CFD domain. To do this, two plenums are considered at the orifice inlet and outlet, each one having a diameter and an axial length ten times larger than the orifice diameter. Thanks to the axial symmetry of the geometry and of the boundary conditions, it is possible to account only for a 5° sector of the whole domain, and to simulate the experiments as two dimensional cases. Fig. 6 shows an example of the CFD domain used. The simulations accounted for three orifice diameters (i.e. 0.5, 1 and 2 mm), three aspect ratios (i.e. 1, 5 and 20) and different Reynolds numbers. The complete list of the simulations, together with their main features, is detailed in Table 2.

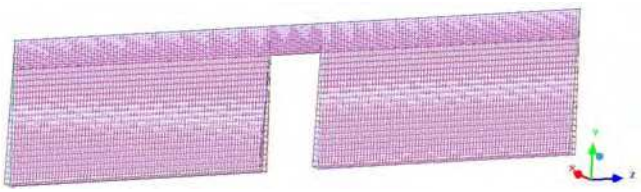

Fig. 6. CFD domain for the small sharp-edged cylindrical orifice test case

Case #	Section diameter	l/d	Reynolds number	Turbulence Model
B_1; B_4; B_7	0.5; 1.0; 2.0 mm	1	5x103; 1x104; 2x104	KE
B_2; B_5; B_8	0.5; 1.0; 2.0 mm	5	1.1x104; 2x104; 4x104	KE
B_3; B_6; B_9	0.5; 1.0; 2.0 mm	20	2x104; 4x104; 6x104	KE
B_10; B_13; B_16	0.5; 1.0; 2.0 mm	1	5x103; 1x104; 2x104	SST
B_11; B_14; B_17	0.5; 1.0; 2.0 mm	5	1.1x104; 2x104; 4x104	SST
B_12; B_15; B_18	0.5; 1.0; 2.0 mm	20	2x104; 4x104; 6x104	SST
B_19; B_22; B_25	0.5; 1.0; 2.0 mm	1	5x103; 1x104; 2x104	LS
B_20; B_23; B_26	0.5; 1.0; 2.0 mm	5	1.1x104; 2x104; 4x104	LS
B_21; B_24; B_27	0.5; 1.0; 2.0 mm	20	2x104; 4x104; 6x104	LS

Table 2. List of simulations for the turbulent flow through a small sharp-edged cylindrical orifice

In the modelling, the above mentioned standard k-ε model, the shear stress transport model and the low Reynolds Launder-Sharma model are compared. Moreover, similarly to the flow through a circular pipe case, different grid resolutions are tested to reduce the grid sensitivity. Finally, a ratio between the radial cell dimension and the orifice radius of 0.02 is found to be a good compromise between computational cost and results accuracy. The

numerical results are compared with measurements mainly in terms of the orifice discharge coefficients. In the experiments the discharge coefficient is calculated using the relation:

$$Q = C_d A_o \sqrt{\frac{2\Delta p}{\rho}} \tag{3}$$

where Δp is the pressure drop across the orifice, ρ the fluid density, A_0 the orifice geometrical area and Q the volumetric flow rate.
Particular care was devoted in calculating the pressure drop and, in order to assess the influence of the abrupt section change only, it was defined as the difference between the inlet static pressure, p_{in} , and the static pressure at the vena contracta position, p_{vc} .

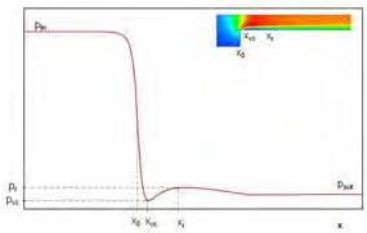

Fig. 7. Axial pressure for the small sharp-edged cylindrical orifice test case

With reference to Fig. 7, the fluid pressure in the vena contracta section, and the axial position of both the vena contracta (x_{vc}) and the reattachment section (x_r) are accurately estimated using the pressure distribution along the orifice length. In particular, the latter parameter is assumed as the axial coordinate of the relative maximum of the pressure profile downstream the vena contracta position. Fig. 8 a) collects, for all the cases reported in Table 3, the comparison between the experimental and the predicted discharge coefficients. As shown, for a given test case and for a wide variation of the Reynolds Number, each graph directly compares the experimental discharge coefficient with the numerical predictions obtained by using all the turbulence models previously depicted. The agreement of the calculated discharge coefficients and the experiments varied significantly among the test cases. The simulations demonstrate a better predictive capability for larger aspect ratios and lower Reynolds number. Under these conditions, the values calculated by using the KE and SST models are sufficiently close to the measured ones. On the other hand, a worse agreement is found for lower aspect ratios. Both turbulence models are able to capture the overall trend of the experiments, even though the SST model demonstrated a better accuracy.
While the behaviour of the KE and SST resulted to be similar, the values calculated by the LS model are found to be significantly different from measurements, and in particular for cases characterized by a small diameter and a low aspect ratio. The tendency of the LS turbulence model of underestimating the velocity close to the wall (highlighted in the flow through a circular pipe analysis also) is therefore confirmed. Consequently, the high turbulent kinetic energy dissipation rate causes a reduced velocity in proximity to the wall, thus forcing a smaller orifice effective area. This behaviour can be noticed also when comparing the axial coordinate of the vena contracta and of the reattaching point calculated by using the three turbulence models (see Fig. 8 b) and c)). A similarity can be noticed for the KE and SST models: while the reattaching points calculated by the LS model result to be

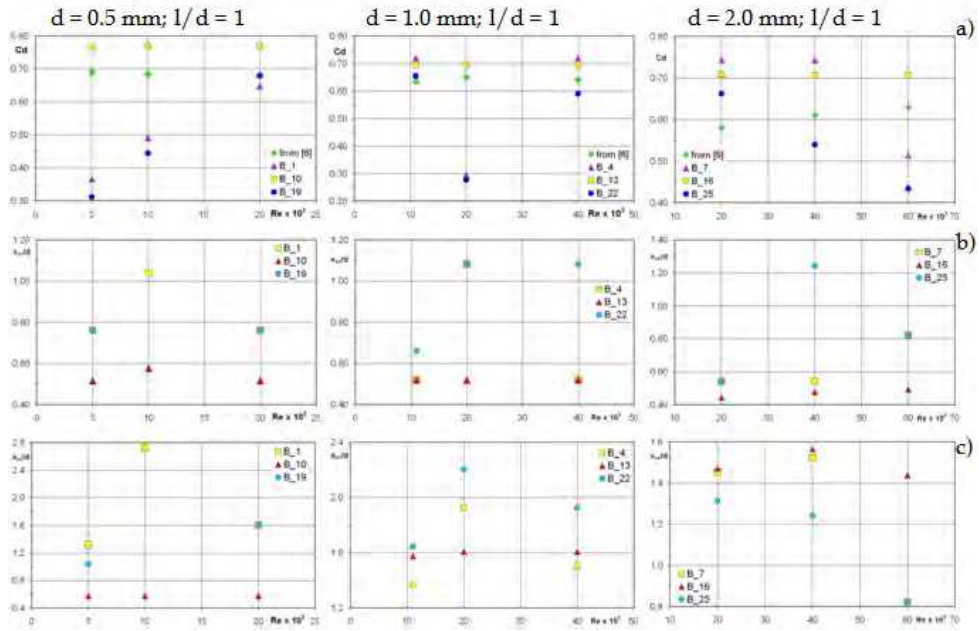

Fig. 8. a) Experimental and calculated discharge coefficients and axial coordinate of b)the vena contracta position and c) the reattaching point for different Reynolds number

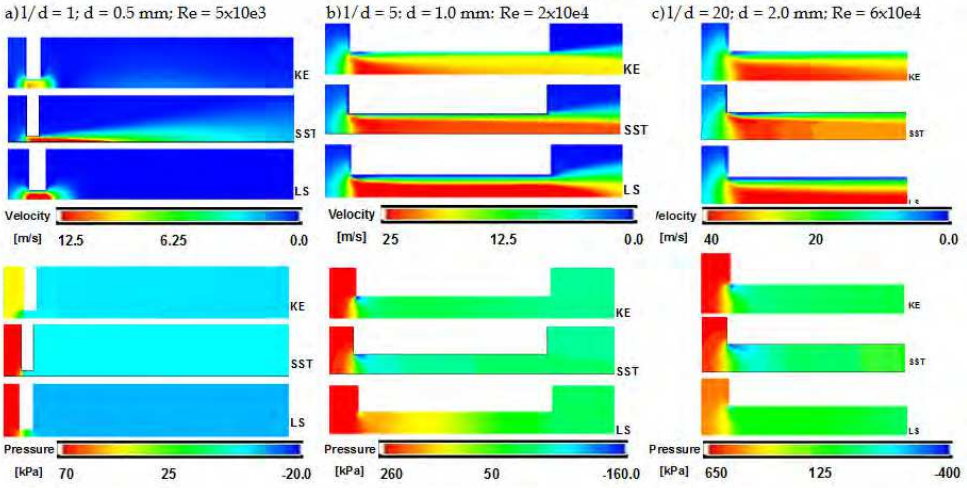

Fig. 9. Turbulence models influence on the velocity magnitude and pressure distribution

more distant from the orifice inlet. In many cases the relative maximum in the pressure profile along the geometry axis is found to be downstream the orifice outlet. This behaviour can be explained by investigating the velocity and pressure distribution along the channel

(see Figs. 9). Finally, it is possible to conclude that the standard k-ε model and the k–ω shear stress transport models demonstrate a sufficient accuracy in calculating the discharge coefficients for most of the analyzed cases. Contrarily, the low Reynolds Launder-Sharma model is found to overestimate the turbulent kinetic energy dissipation, particularly in the wall proximity, thus causing an underestimation in the orifice effective area prediction. For the small diameter and low aspect ratio cases, the cavitating phenomena cannot be neglected in order to predict with a reasonable accuracy the discharge coefficients.

3. Modelling of cavitation and aeration

Once the predictive capabilities of the numerical models for the simulation of the incompressible flow are investigated, further step of the analysis is the modelling of the cavitation and aeration phenomena. The cavitation model used in this work is based on a barotropic equation of state approach and it assumes that the two phases (gas and liquid) have equal velocities and temperatures at any point of the flow (i.e. homogeneous equilibrium) (Yadigaroglu & Lahey, 1976). The assumption of isothermal flow is also made. The selected barotropic equation used in the modelling reads as follows:

$$\frac{d\rho}{dt} = \psi \frac{dp}{dt} \tag{4}$$

where ψ is the mixture compressibility. The parameter that accounts for the amount of fluid which is in the liquid or gaseous phase is the following:

$$\gamma = \frac{\rho - \rho_{l,sat}}{\rho_{ref} - \rho_{l,sat}} \tag{5}$$

where the reference gas density (ρ) is determined as the maximum value between the vapour density of the liquid fluid and the dissolved gas density at the current local pressure. The amount of dissolved gases which are locally released is calculated by introducing the Henry law for the equilibrium condition and accounting for the time dependence of solubility on a Bunsen coefficient basis. The released gas amount is firstly calculated from Henry law and the initial volume fraction of dissolved gas. The influence of time on gas absorption and dissolution is then accounted for by means of the Bunsen coefficient, c_B; thus the time variation of the released gas volume fraction, ε_c, can be calculated as follows (Weiss, 1970; Zarotti, 1998; Payri et al., 2002):

$$\frac{d\varepsilon_c}{dt} = \frac{\varepsilon - c_B p - \varepsilon_c}{\tau_c} \tag{6}$$

where ε is the gas – liquid saturated mass ratio, and τ_c is the time constant of the absorption or dissolution of the gas into the liquid medium. The Bunsen coefficient can range approximately from 0.02 for water to 0.09 for mineral oil (Zarotti, 1998), while it is very difficult to find in literature typical values of the time constant τ_c. Unfortunately, this lack of data is a stringent restriction for the gas release estimation. In fact, the amount of gas released during an expansion process is greatly influenced by the time constant, as well as the amount of gas which is dissolved during compression. Fig. 10 shows the volume fraction

between the released gas and the liquid during an expansion from 1 bar to the liquid vapour pressure, a settling phase and a subsequent compression back to 1 bar. The time for the expansion and compression phases is set to 0.2 s while the settling phase is equal to 0.8 s.

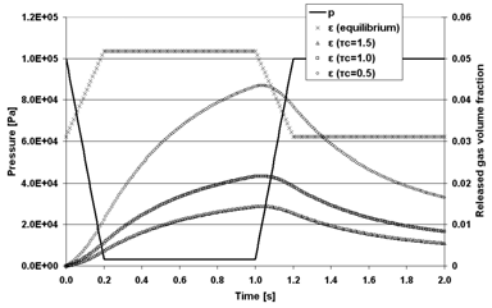

Fig. 10. Released gas volume fraction during an expansion and compression cycle

Different time constants are compared, and it is possible to notice that the released gas volume fraction is far from the equilibrium value both for the expansion and the compression processes. Thus, the released gas is not dissolved immediately and it lasts for a time period comparable with the process itself. The CFD analysis is carried out by means of the open source computational fluid dynamics code OpenFOAM. Bounded central differencing is used for the discretization of the momentum, second-order upwind for subgrid kinetic energy, and the mixture fraction. Pressure–velocity coupling is achieved via a Pressure Implicit Splitting of Operator algorithm similar procedure. The second-order implicit method is used for time integration scheme. The cavitation model originally implemented in OpenFOAM code does not account for the effects of turbulence. Therefore, the code is modified in order to account for the turbulence in the compressible flow equations. The approach to turbulence modelling is simplified since the effects of the liquid – gas/vapour interface are neglected, and this point remains an area for further investigation. In all the simulations carried out for the present work the turbulence is modelled by means of the two zonal version of the k-ω model, known as the shear stress transport model (Menter, 1993). The grids used in the simulations are constructed paying careful attention to comply with the requirements on the y^+ values for the k- ω SST formulation. Finally, the liquid and gaseous phase is tracked by using the volume of fluid (VOF) method where both fluid phases are compressible. The numerical approach is preliminarily validated by simulating a test case available in literature (Ramamurthi & Nandakumar, 1999) and comparing the numerical results with the experimental measurements. The selected geometry is a sharp-edged cylindrical orifice and the working fluid is water. The properties of water used in the simulations are the standard values at the reference temperature of 293 K. The dissolved gas fraction is assumed equal to the average value for tap water at ambient pressure, i.e. 0.01%. In the experiments the effects of varying the diameters of the sharp-edge orifice and the ratio of the inlet diameter (d) and the orifice length (l) are investigated for different Reynolds numbers of operation. The modelling of the experimental device focuses only on the orifice geometry, and particular care is paid to assure that the flow at the orifice extremes is not influenced by the inlet and outlet of the CFD domain. To do this, two plenums are considered at the orifice inlet and outlet, each one

Fig. 11. CFD domain for the small sharp-edged cylindrical orifice case (d=1 and l/d = 20)

Section diameter	l/d	Reynolds number
0.5 mm	20	4.5x103; 1.1x104; 1.8x104
0.5 mm	50	5.9x103;8.5x104; 1.2x104
1.0 mm	20	1.1x104;1.8x104; 3.4x104
1.0 mm	50	8.8x104; 12.6x104; 3.3x104
2.0 mm	20	3.4x104; 4.9x104; 7.2x104
2.0 mm	50	1.2x104; 3.4x104; 5.6x104

Table 3. Test cases for the flow through a small sharp-edged cylindrical orifice

having a diameter and an axial length ten times larger than the orifice diameter. Thanks to the axial symmetry of the geometry and of the boundary conditions, it is possible to account only for a 5° sector of the whole domain, and to simulate the experiments as two dimensional cases. Fig. 11 shows an example of the CFD domain used. The present analysis focuses only on the geometrical configurations and operating conditions where cavitation was evidenced by the experiments in (Ramamurthi & Nandakumar, 1999). Table 3 details the test cases that are accounted for in the simulations. The numerical results are compared with measurements mainly in terms of the orifice discharge coefficients calculate as described in section 2.2. In order to evaluate the influence of cavitation and aeration modelling on the results' accuracy, the test cases are simulated by means of three different numerical approaches to cavitating flows analysis, i. e. a numerical approach which accounts for turbulent flows but does not include any cavitation model, a second approach which includes the cavitation model but assumes the flow as laminar and a third numerical approach with accounts both for turbulence and cavitation. Evidently, the computational cost increases from the first approach to the last one, and the accuracy of the results which can be obtained depends on the single problem that has to be simulated. Therefore, the predictive capabilities of the above mentioned numerical approaches are addressed when simulating cavitating flows. Fig. 12 shows the comparison between the experiments and calculations for the selected test case in terms of discharge coefficients. In the Figure the trend of the discharge coefficients in case of attached flow is also plotted (dotted line). This line represents the limit between the hydraulic flip cases and the reattached flow conditions. All the numerical approaches used in the simulation demonstrate to predict the discharge coefficient trend as a function of the Reynolds number. Nevertheless, the results' accuracy increases when adopting a cavitation model. In fact, when comparing Fig. 12 a) and c) and Fig. 12 b) and c) respectively, it can be noticed that better agreement between measurements

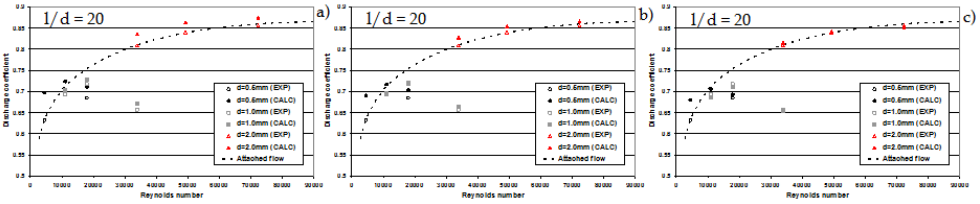

Fig. 12. Comparison between measured and calculated discharge coefficients for simulations a) without cavitation model and turbulent flow, b) with cavitation model and laminar assumption and c) with cavitation model and turbulent flow

and calculations can be achieved by the simulations accounting for cavitation and neglecting the turbulence effects. Thus, in order to improve the predictive capabilities of hydraulic components analysis, modelling the cavitating regions results to be more important than accounting for turbulence effects, when considering all the operating conditions used in the selected test cases,. This behaviour confirms what has been evidenced in (De Villiers, 2004) for the numerical analysis of the injector nozzle flow. In particular, in the simulations without any cavitation model, the low pressure regions immediately downstream the abrupt section change are underestimated (see Fig. 13). This behaviour can be explained by the fact that the velocity variation affects only pressure, while in the numerical analysis accounting for cavitation both pressure and density vary with velocity. As can be expected, the results' accuracy can be further improved by accounting both for the cavitation and the turbulence effects. Fig. 12 c) demonstrates that a better agreement between the measured and calculated discharge coefficients can be obtained by adopting the third numerical approach. When comparing the flow field obtained by the numerical approach with cavitation model and laminar assumption and the one with both cavitation model and turbulent flow no remarkable differences can be noticed within the orifice. The low pressure region downstream the abrupt section change results to be slightly larger for the former approach. In Fig14 the void fraction calculated by the numerical approaches without and with turbulence model is compared. It can be noticed that the gamma distribution is very

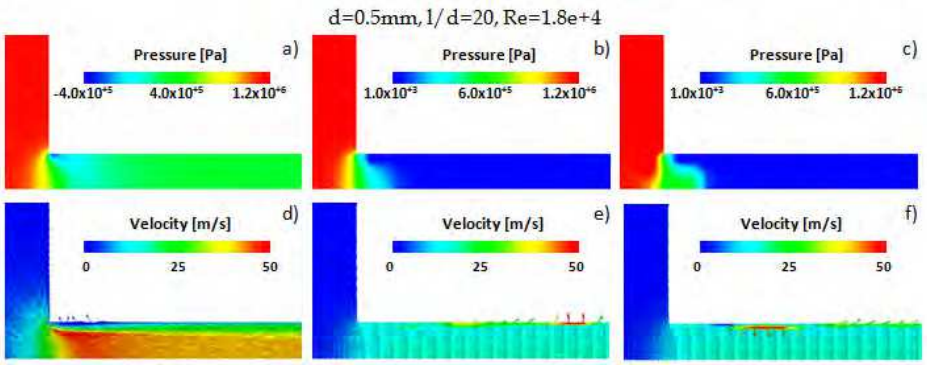

Fig. 13. Pressure and velocity distribution on a cut plane through the cylinder axis for different approaches: a) and d) no cavitation model and turbulent flow, b) and e) with cavitation model and laminar flow and c) and f) with cavitation model and turbulent flow

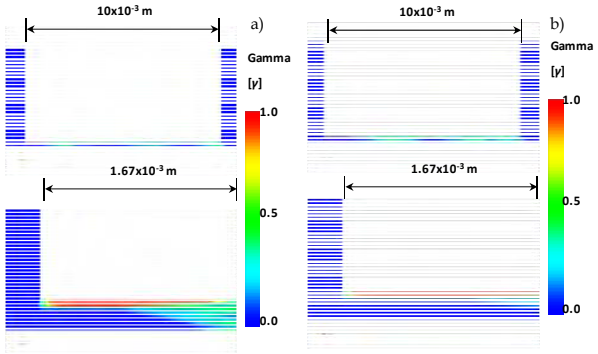

Fig. 14. Void fraction distribution on a cut section through the cylinder axis for a numerical approach with cavitation model: a) laminar assumption and b) turbulent flow

similar between the two models; nevertheless, when accounting for turbulence the gas/vapour phase is slightly more dispersed and it propagates closer to the cylinder axis. As can be seen in Fig. 12 for the case having orifice diameter equal to 0.5 mm, l/d = 50 and Reynolds Number of $1.8x10^4$ the flow does not reattach in the orifice. This behaviour is clearly evidenced by the gamma distribution in Fig. 14. Gas/vapour phase results to be distributed all through the orifice until the flow reaches the outlet plenum.

4. Steady state modelling of hydraulic components

The numerical models described in the previous sections are now adopted for the analysis of a specific hydraulic component: a closed centre electro-hydraulic load-sensing proportional control valve, usually adopted in multi-slice blocks to control parallel actuations of industrial, agricultural and earthmoving applications. In particular, the numerical simulation is used to evaluate the valve performance in terms of overall discharge coefficient, efflux angle, flow forces and pressure and velocity distributions in the critical region. In its simpler design, the proportional control valve for load-sensing applications is intended to directly react to a pressure signal (coming from the actuator) in order to maintain as constant as possible the pressure drop across its metering edges. This action is normally influenced by a local pressure compensator which could have either a single or a double stage configuration, and is usually placed upstream or downstream the control valve centre. Therefore, for a given operating position of the control valve spool, and for the flow-rate across the efflux area of metering orifices the pressure drop can be maintained constant independently by the actuator work-load. Fig. 15 depicts the closed centre load-sensing proportional control valve studied here. It is designed for operational field limits up to 100 l/min as maximum flow-rate and up to 350 bar as maximum pressure. As shown, the centre presents a Z connection between the high pressure port (P, in red) and the internal volume (P1, magenta), which is metered in all spool directions by a twice notched edge. At the same time, both connections between the internal volume and the actuator ports (A and B, green), and those between the actuators ports and the discharge line ports (T, blue) are metered by multiple notched edges. It is worth mentioning that the central volume indicated as P1 normally hosts the local pressure compensator (not included in the sketch in Fig. 15). The Figure presents also a view of the proportional control valve spool including a zoomed view

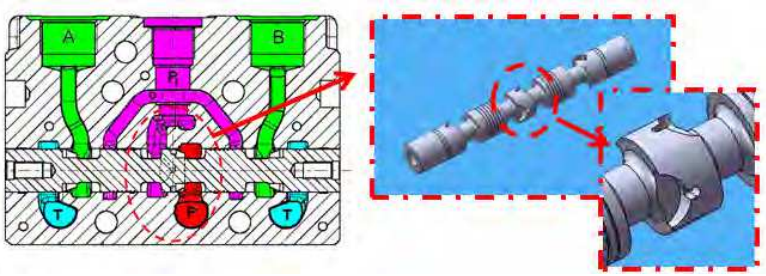

Fig. 15. Main section of the control valve and view of the spool's metering edges

of the design of the central edge. As shown, two equal notches located at 180° characterize each side of the central edge, and each couple of notches has a 90° rotation with respect to the other one. Moreover, the notches on the left side of the central edge meter the hydraulic power during the spool motion from the centre to the right (when P1 opens to A, and B opens to T), while the notches on the right side works during the motion from the centre to the left (when P1 opens to B, and A opens to T). In this way, the high pressure port P is connected to the control valve internal volume through an asymmetric path, which depends on the spool direction of motion. The CFD domain used in the simulations, see Fig. 16, includes the metering edges of the proportional control valve (upper, lower, front and back notch), the inlet duct and the outlet region up to the central volume where usually a local pressure compensator is positioned. The considered domain is marked with a dashed line in Fig. 15. The corresponding mesh is created using an unstructured grid paying particular care to the metering areas. Local refinements are used to obtain a large number of cells in the critical sections and at small opening positions. Moreover, wall cell layers are employed in order to have the proper wall cell height accordingly to the adopted turbulence model. The average mesh resolution is set to 0.3 mm corresponding to an overall cell number equal to 3 million elements. Fig. 16 b) shows the mesh of the zoomed views of a the metering edge. In the numerical analysis, several spool positions are considered in order to simulate different operating conditions of the control valve. In particular five spool displacements are investigated when the inlet and outlet regions are connected by means of the upper and lower notches (i.e. direct flow through the notches) and the corresponding five spool displacements in which the front and back notches connect the inlet and outlet of the valve (i.e. inverse flow through the notches). The former spool positions are considered as positive while the latter ones are assumed as negative even though the opening area is the same, since the spool displacement is symmetric with respect to the valve centre. Table 4 details all the operating conditions used in the analysis. As can be noticed from the Reynolds number listed in Table 4, all the cases are fully turbulent. Therefore, in the simulations carried out for the present work the turbulence is modelled by means of the two zonal version of the k-ω model, known as the shear stress transport model. Furthermore, careful attention is paid in order to comply with the requirements of the turbulence model adopted. The results of the numerical analysis of the load-sensing proportional control valve are discussed in terms of discharge coefficients, pressure and velocity fields, flow forces and flow acceleration angles. In particular the effect of the direct and inverse flow through the notches is highlighted. Fig. 17 a) depicts the comparison between the reference and calculated inlet pressures. In the simulations the outlet pressure is assumed as a constant boundary condition, while the inlet

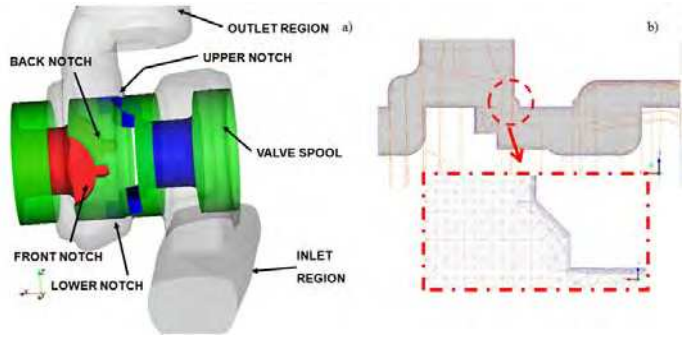

Fig. 16. a) The geometry of the control valve included in the CFD domain and b) detail of the mesh in the notch region for a mid range opening position of the spool

	Spool displacement (x/xmax)	Reynolds number
Inverse flow through the front and back notches	-1.00	3573
	-0.78	4209
	-0.65	3289
	-0.50	2174
	-0.35	1422
Direct flow through the upper and lower notches	0.35	1423
	0.50	2176
	0.65	3290
	0.78	4210
	1.00	3561

Table 4. Spool displacements and operating conditions used in the simulations

pressure is calculated as a consequence of the fluid – dynamics losses through the metering edges. As a first result, it can be noticed that even though the boundary conditions are symmetrical with respect to the control valve centre, the predicted inlet pressure is slightly different when comparing the direct and inverse flow. This behaviour is more evident when comparing the discharge coefficients, see Fig. 17 b). The discrepancy can be attributed to two main reasons. First, in the direct flow (i.e. positive spool displacements) the effective area decreases progressively as the liquid flows through the notches up to the vena contracta section close to the notch outlet; conversely, in the inverse flow, the area decreases abruptly at the notch entrance. Second, the front and back notches have very similar geometrical boundaries both at the inlet and at the outlet, while the geometrical volumes downstream the upper and lower notches differ significantly. In fact the liquid flowing out from the upper notches is heading for the outlet boundary, whilst the flow out from the lower notch finds a confined region causing further pressure losses. These reasons have opposite effects on the discharge coefficient; in fact the first one would advantage the direct flow while the second reason would advantage the inverse flow. The numerical simulations show that the trade-off between these two contrasting trends results in a better discharge coefficient for the inverse flow. This behaviour is also confirmed when comparing the flow

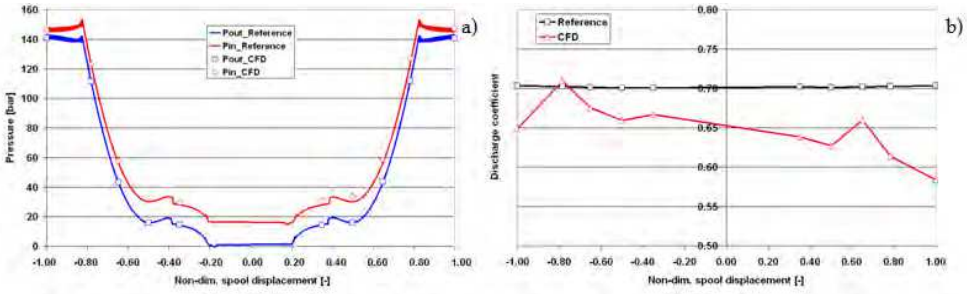

Fig. 17. Comparison a) between reference and calculated pressures at the valve inlet and outlet and b) between reference and calculated discharge coefficients

fields obtained for the different operating conditions. As an example, Fig. 18 plots the pressure and velocity fields on a cut section through the symmetry plane of the front and back notches (inverse flow) and the upper and lower notches (direct flow) for a small displacement case. While the flow through the front and back notches look very similar, the pressure and velocity fields are significantly different for the upper notch and the lower notch. In particular, the flow exiting the lower edge hits the outlet chamber wall and bounces back into the spool volume and then it is redirected to the outlet boundary. This

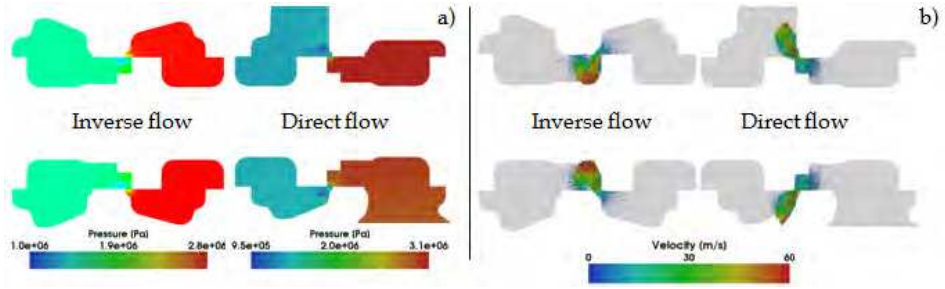

Fig. 18. a) Pressure and b) velocity distributions on a cut section through the symmetry plane of the metering section for the inverse and direct flow (x/x_{max}=0.35).

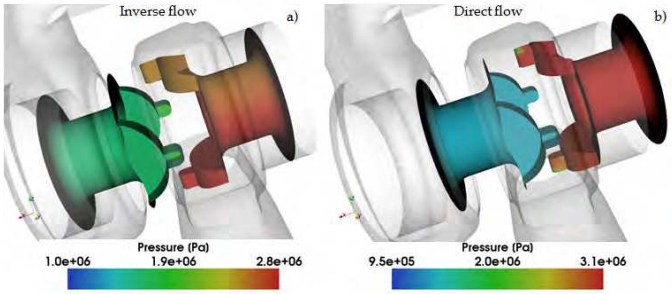

Fig. 19. Pressure distributions on the spool chambers used for the calculation of the flow forces for a) the inverse flow and b) the direct flow)

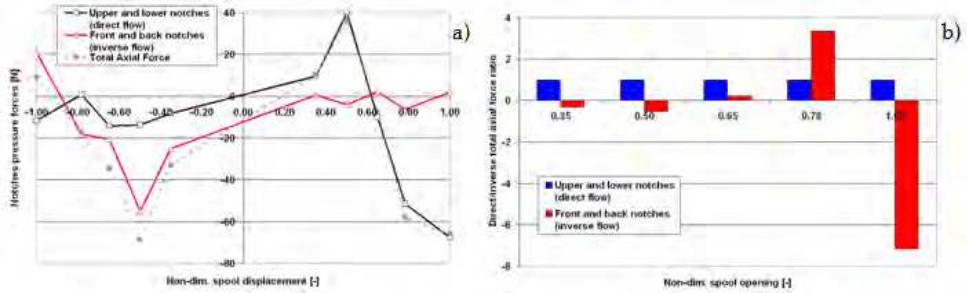

Fig. 20. a) Flow forces exerted on the valve spool in the axial direction and b) ratio between the total axial flow forces in case of direct and inverse flow

more complicated flow pattern increases the fluid – dynamics losses and thus determines a smaller discharge coefficient. By integrating the pressure distribution over the surface of the spool chambers' walls, it is also possible to calculate the axial forces exerted on the spool by the flow. Fig. 19 depicts the pressure contours on the walls of the spool chambers for all notches both in case of direct and inverse flow (as an example only the case with x/x_{max}=0.35 is plotted). It can be noticed that the pressure contour is quite uniform for the non operational notches, while the pressure varies significantly throughout the walls of the notches through which the oil flows. This behaviour results in a very low integrated value of the flow induced forces on the non operational chamber of the spool, as can be seen in Fig. 20. When comparing the integrated values of the forces for the direct flow (upper and lower notches) and the inverse flow (front and back notches), it is possible to outline that the behaviour is clearly not symmetrical with respect to the control valve centre, see Fig. 20 a). In fact, even though the trend looks similar and in both cases the sign of the forces reverses moving from the small to the large displacements, the magnitude is rather different. Fig. 20 b) details the ratio between the total axial forces obtained in case of direct and inverse flow. The forces have the same sign only at mid range displacements and the inverse flow induced forces are initially lower than the direct flow ones but approaching the maximum displacement they become much larger. Finally, by using the average velocity vector at the exit of the four notches it is possible to estimate the flow acceleration angle for each metering edge. Fig. 21 shows the convention used in this analysis for the calculation of the efflux angle with respect to the coordinate system axes. When values larger than 90 degrees are found, the negative supplementary angle is considered. Fig. 22 a) shows the efflux angles for the four metering sections as a function of the spool displacement. The angles are calculated for each notch only in its operational spool opening range. It is interesting to notice that each couple of notches has a quite similar behaviour. While this result could be expected for the front and back notches due to their similar geometrical boundaries, it is less evident in the case of the direct flow, where the downstream region is very different for the upper and lower notches. Furthermore, when comparing the efflux angles obtained for the direct and inverse flows, it can be remarked that the trend looks similar. In fact, smaller angles are characterizing the small spool displacements, as a consequence of the Coanda effect, whereas they are increasing moving towards the maximum opening. Nevertheless, in the average the direct flow results in larger flow acceleration angles; this behaviour is likely due to the fact that the main flow direction change happens close to the notch exit, while in the inverse flow the stream bends abruptly just entering the notch. By knowing the flow

acceleration angles it is then possible to calculate the theoretical values of the axial forces, F_{th}, through the von Mises theory:

$$F_{th} = -2 \cdot C_d \cdot C_v \cdot \cos\varphi \cdot \Delta p \cdot A \tag{7}$$

where C_d and C_v are the discharge coefficient and the velocity coefficient (in the following assumed equal to 0.98), Δp is the pressure drop across the metering edge, A is its geometrical area and φ is the efflux angle. Fig. 22 b) depicts the comparison between the theoretical flow force and the one predicted by using the numerical simulation (grey lines). In the CFD results, the contributions of each metering edge are also plotted (red and black lines). The theoretical calculations and the numerical predictions are significantly different, and in particular by using the von Mises theory it is not possible to determine the change of direction moving from low to high spool displacements both for the inverse and direct flow.

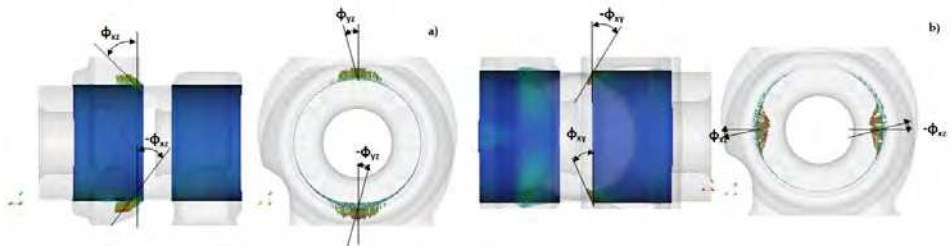

Fig. 21. Convention used for the calculation of the efflux angles

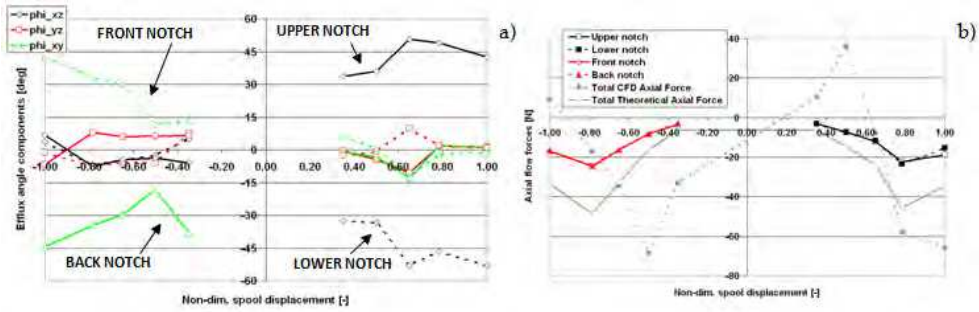

Fig. 22. a) Efflux angles for the different notches as a function of the spool displacement and b) comparison between theoretical and predicted axial forces

5. Fully transient modelling of hydraulic components

The numerical analysis of the hydraulic valve addressed in the previous section is further deepened by adopting a fully transient numerical approach. The main issue in this type of analysis is the moving mesh methodology employed to simulate the spool displacement profile versus time. To accomplish this task, the mesh changer libraries of the OpenFOAM code are modified to account for the linear motion of a portion of the geometry sliding over a second portion. The mesh motion is resolved by using a Generalized Grid Interface (GGI)

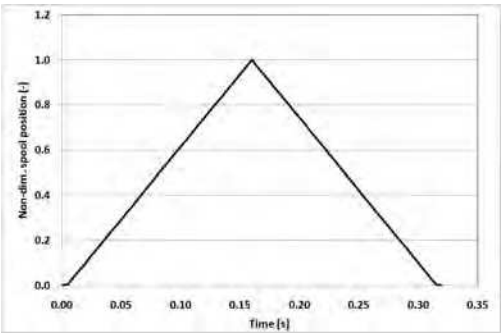

Fig. 23. PWM control applied to the spool motion

approach (Beaudoin & Jasak, 2008), originally developed for turbomachinery applications and modified to include not only rotational motion of the moving grid but also the linear displacement of a valve spool. The spool is moved accordingly to the PWM control profile depicted in Fig. 23. The other models adopted in the analysis are the same as the ones detailed in the previous sections. The valve is tested under several operating conditions. In particular, three constant flow rates at the inlet are considered, while a forth case is accounted for, in which the pressure across the valve is held constant. The four cases are first simulated by using a steady state approach and then a full transient approach. For the steady state simulations, four spool displacements are studied spanning from an almost closed position to mid range and maximum displacement. In case of steady state analysis there is no difference between the opening and the closing travels; on the contrary for the transient approach different inertia phenomena may arise. Table 5 lists the simulated cases, detailing the steady states and transient simulations. The comparison between the results obtained by the steady state calculations and the fully transient ones are discussed in terms of total pressure drop across the component, discharge coefficients, pressure and velocity fields, and flow acceleration angles. In Fig. 24 a) the total pressure drop across the valve is depicted for Cases # 1 to 3 and Cases # 5 to 7. The values predicted by the steady state calculations and the transient ones do not differ remarkably; particularly in the transient simulations the pressure variation during the opening and closing travels are quite similar. A large discrepancy can be seen when considering constant pressure at the boundaries. Fig. 24 b) plots the flow rate through the valve when holding constant the pressure drop across the component, i.e. 20 bar. The values predicted by the steady state simulations at small spool displacements are very close to the ones calculated during the opening phase with the transient approach. At large spool displacement the saturation flow rate resulted to be lower for the transient approach than for the steady state simulation. It is interesting to notice the difference between the flow rate calculated during the opening and the closure of the spool. The inertia of the flow through the metering edge of the valve causes a small fluctuation as the spool reverses it direction, while at mid range displacements the difference is even more evident. During this part of the metering curve, the flow inertia is being opposing to the spool motion and the total effect is a larger fluid dynamics loss. Similar behaviour can be seen also when considering the discharge coefficients, see Figs. 25 and 26. When the flow rate is held constant, the values during the first part of the opening travel are slightly larger than the ones during

	Inlet condition	Outlet condition	Spool positions	Numerical approach
Case #1	Constant flow rate (Q=12 l/min)	Constant pressure (pout=50 bar)	0.038; 0.35; 0.68; 1.00	Steady state simulations
Case #2	Constant flow rate (Q=30 l/min)	Constant pressure (pout=50 bar)	0.038; 0.35; 0.68; 1.00	Steady state simulations
Case #3	Constant flow rate (Q=100 l/min)	Constant pressure (pout=50 bar)	0.038; 0.35; 0.68; 1.00	Steady state simulations
Case #4	Constant pressure (pin=70 bar)	Constant pressure (pout=50 bar)	0.038; 0.35; 0.68; 1.00	Steady state simulations
Case #5	Constant flow rate (Q=12 l/min)	Constant pressure (pout=50 bar)	Function of time (see Fig. 25)	Transient simulation
Case #6	Constant flow rate (Q=30 l/min)	Constant pressure (pout=50 bar)	Function of time (see Fig. 25)	Transient simulation
Case #7	Constant flow rate (Q=100 l/min)	Constant pressure (pout=50 bar)	Function of time (see Fig. 25)	Transient simulation
Case #8	Constant pressure (pin=70 bar)	Constant pressure (pout=50 bar)	Function of time (see Fig. 25)	Transient simulation

Table 5. Boundary conditions used for the different simulated cases

closure, while as the direction reverses the discharge coefficients are larger due to the inertia, but decreases remarkably as the metering edge reduces as an effect of the larger losses. When comparing the discharge coefficients calculated by the steady state and transient approach, the values are quite close, particularly at large spool displacement and for the opening travel. Conversely, if the values during the closure travel are considered, the transient simulations predict lower discharge coefficients as a results of the behaviour mentioned before. Figs. 25 and 26 plot also the efflux angle for the different cases. The efflux angle is calculated accordingly to the reference system mentioned in section 4. A common trend of the efflux angle is predicted for all the transient simulations. The angle tends to increase rapidly during the small spool displacements reaching a local maximum between 0.5 and 1.5 mm, ranging from small to large flow rate, while it decreases during the mid range displacements and finally it starts increasing again at high spool axial positions. The efflux angle results to be slightly larger for the closure travel all through the displacements; the flow exiting the metering section during the closure phase results to be more disperse when compared to the flow during the opening travel. This behaviour is clearly visible when considering the flow field during the opening and closure travels, see Fig. 27. The efflux angle trend described above for the transient simulations is definitively different from the behaviour predicted by the steady state calculations; in fact, with the steady state approach the efflux angle is increasing as the spool displacements increases. Furthermore, the efflux angle values calculated by this approach resulted to be larger than the ones obtained with the transient simulations. This difference has a remarkable importance if the flow forces are accounted for, since they are significantly affected by the vena contracta angle.

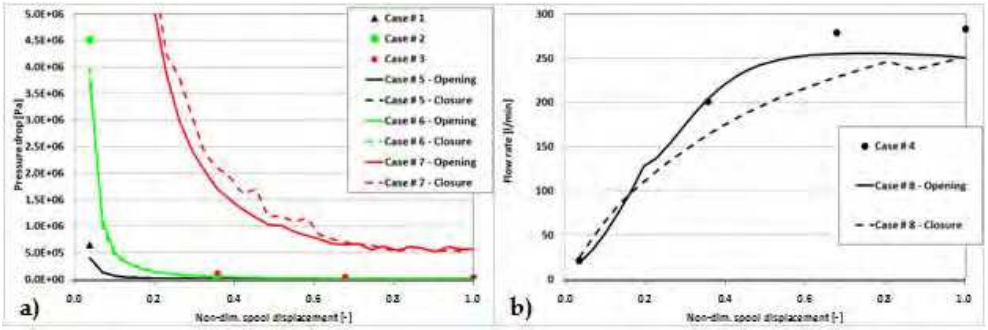

Fig. 24. Comparison between the a) pressure drop and b) flow rate through the metering area predicted by the steady state and transient simulations.

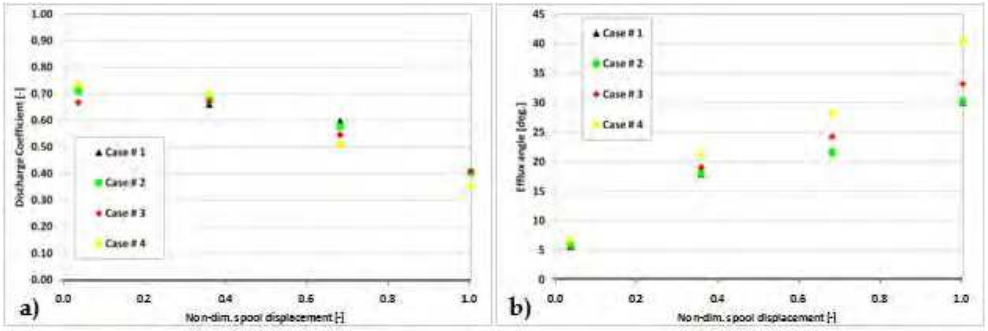

Fig. 25. a) Discharge coefficients and b) efflux angle for the steady state simulations

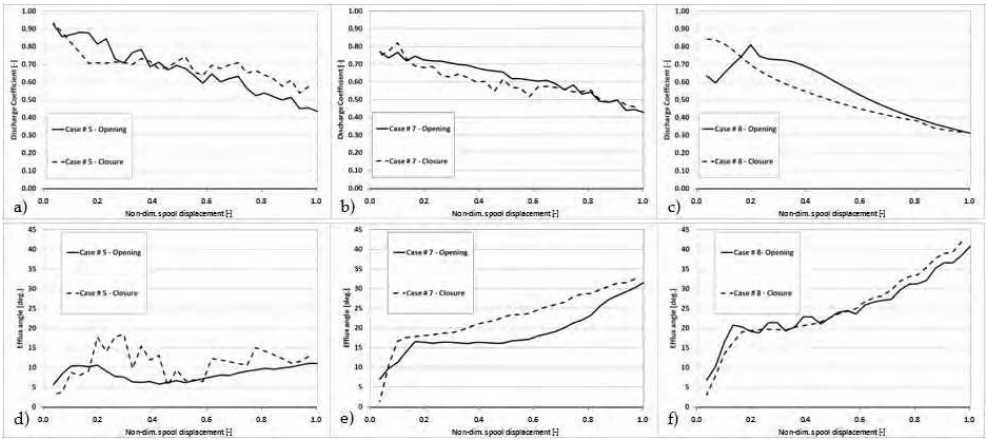

Fig. 26. a), b) and c) Discharge coefficient and d), e) and f) efflux angle for the transient cases

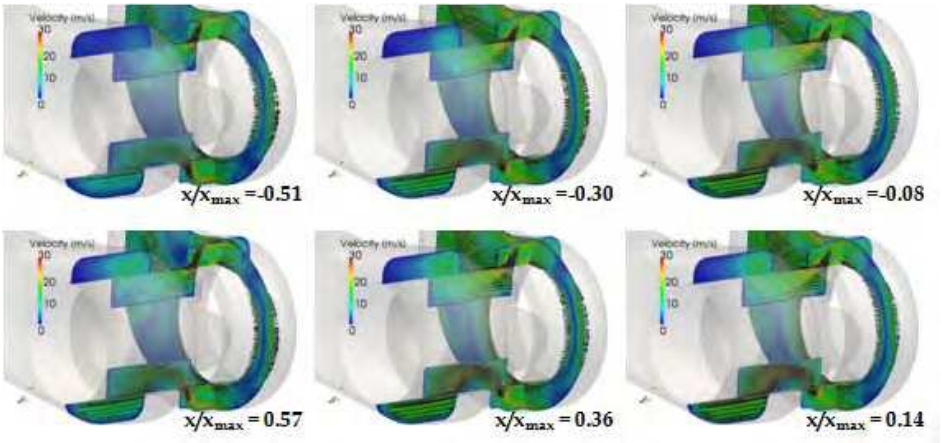

Fig. 27. Velocity distribution for different non-dim. spool displacements (Case # 7)

6. Modelling approach for a multi-fuel injection system

The numerical approach described in the previous section for the design and performance prediction of hydraulic components is employed for the analysis of a low pressure, common rail, multi-fuel injection system. In particular, system is working with a mean pressure close to 3.5 bar and every injector is driven by a modified PWM control characterized by 3rd order function opening and closing ramps and characteristic times adapted to the engine rotational speed through an ECU correction. In the numerical analysis of this hydraulic system, the turbulence as well as the cavitation models are used to address the flow within the injector in order to estimate the permeability characteristics of the injector when operating with different fuels. In the analysis, the operating conditions for the injectors are preliminarily evaluated by lumped and distributed parameter approach. Thus, the system behaviour and the injection profiles for several fuel blends are calculated. The general reliability of the one-dimension approach is defined with respect to experimental data mainly in terms of injected mass per stroke. Fig. 28 shows the injection system model including only the rail and the injectors. The connection to the supply is simplified by means of a flow-rate source. The Figure shows also the injector lift and the modified PWM wave; the total time, t_{inj}, is adjusted accordingly to the measurements. The CFD analysis focuses only on the injector geometry since it represents the main component influencing the permeability of the hydraulic system. The injector is characterized by six nozzles: the first one is in-line with the injector axis, while the other five are located circularly every 72 degrees. Therefore, the injector geometry and the boundary conditions are cyclic symmetrical allowing the simulations to be carried out only over a 72 degree sector mesh (see Fig. 29). In the simulations the pressure at the nozzles' exit is kept constant equal to 1 bar, while the inlet pressure is varied from 3.5, 5 and 10 bar. In fact, the lowest inlet pressure is the current injection pressure for this type of multi – fuel injection system, but the tendency is to increase it in order to comply with the mass flow rate required by new fuels and new injection strategies. Finally three different fuels are accounted for in the numerical analysis. Simulations with varying needle lifts and injection pressures are carried out for pure ethanol, pure gasoline and a fuel mixture corresponding to 50% gasoline and 50%

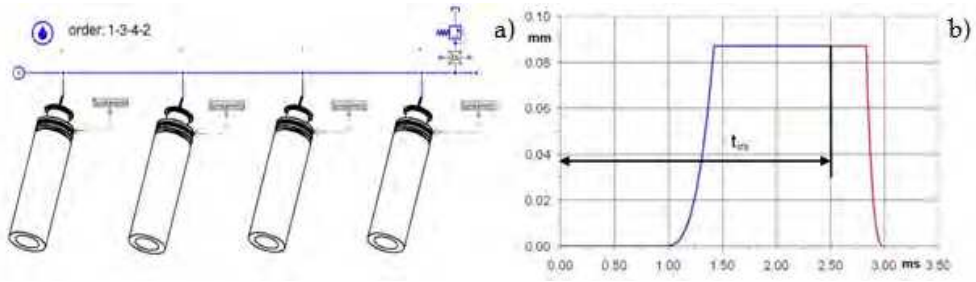

Fig. 28. a) Layout oft he lumped and distributed parameter model and b) modified PWM control applied to the injector lift

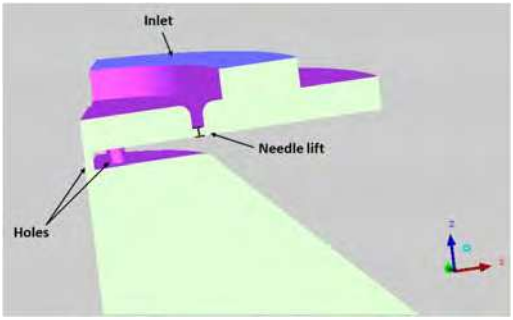

Fig. 29. Geometry of the 6 nozzle injector tip used in the simulation (72 degree sector)

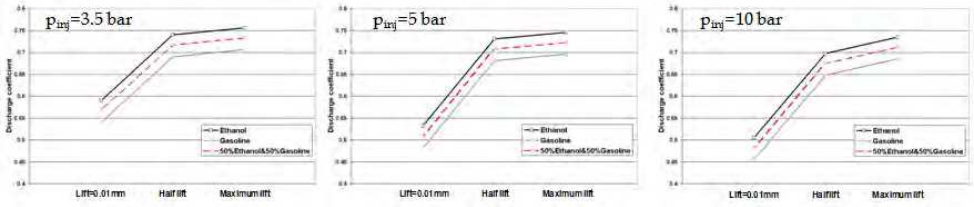

Fig. 30. Discharge coefficient vs. needle lift for different fuels

ethanol in terms of mass fraction. Fig. 30 shows the performance of the injection system in terms of discharge coefficients as a function of the lift, injection pressure and operating fuel. In all simulations the back pressure at the outlet was assumed to be constant at 1 bar. When comparing the results holding constant the injection pressure, it is possible to highlight that, as expected, the discharge coefficients for the maximum and half lifts are very similar and only for the almost closed position it reduces drastically. When considering the influence of

the working fuel a significant difference can be seen for all the injection pressures and needle lifts. In fact, the discharge coefficients tend to decrease remarkably when injecting gasoline. The reduction reaches values up to 7% when compared to ethanol injection and the trend is rather homogeneous for all the considered cases. This result can be attributed to the different vapour pressure for ethanol and gasoline; the higher vapour pressure allows the fuel to vaporize earlier causing larger low density regions within the nozzle. This effect can be seen as a reduction of the effective area of the nozzle throat section. This behaviour can be clearly evidenced when considering the flow field within the injector nozzle in terms of pressure and void fraction distributions (see Figs. 31 and 32). By comparing the pressure and void fraction contour plots on a cut plane through the nozzles' axes holding constant the working fuel and varying the injection pressure and needle lift, see Fig 31, no relevant differences can be observed in the pressure field when halving the needle lift with the same injection pressure, while a larger low pressure region in both nozzle can be evidenced for the almost closed needle position. Same observation can be made when addressing the void fraction distribution; only at the highest injection pressure a remarkable high vapour fraction region appears. Fig. 32 depicts the results obtained by varying the injected fuel and needle lift while holding constant the injection pressure (i.e. 3.5 bar) in terms of pressure and vapour fraction distributions. As anticipated when describing the results in terms of discharge coefficients, in case of gasoline injection the low pressure regions within the nozzle are wider than in case of ethanol or ethanol/gasoline fuel mixture. Consequently, larger high vapour fraction regions form in the nozzle and close to the nozzle outlet, thus reducing the effective area.

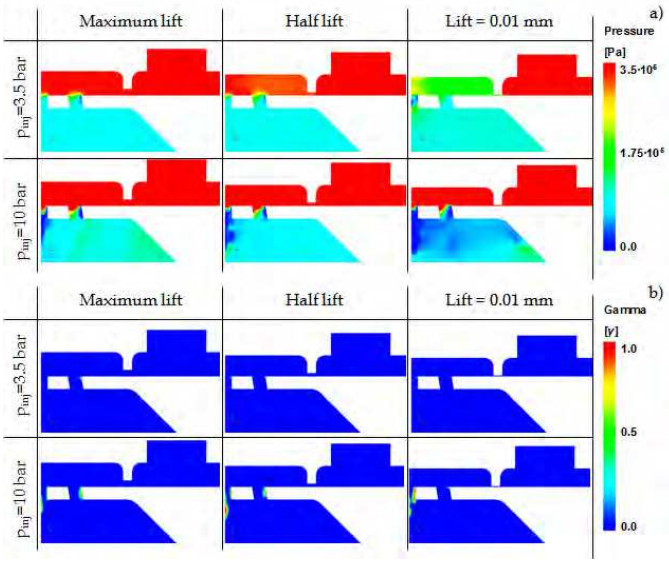

Fig. 31. Comparison of a) the pressure and b) the void fraction (gamma) distributions on a cut section through the nozzles' axes for different injection pressures and needle lifts (injected fuel: ethanol)

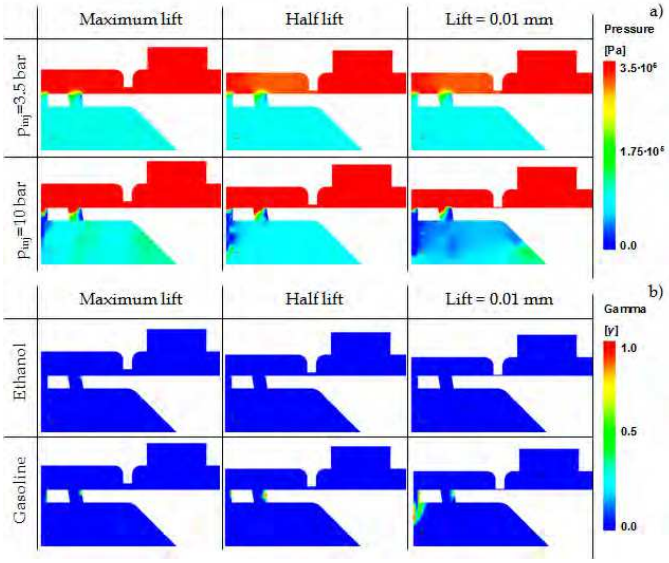

Fig. 32. Comparison of a) the pressure and b) the void fraction (gamma) distributions on a cut section through the nozzles' axes for different injected fuels and needle lifts (injection pressure: 3.5 bar)

7. Conclusion

In this chapter, a numerical approach for the multidimensional design of hydraulic components and systems has been shown. The procedure for setting up the numerical analysis have been highlighted in order to provide the designer with the guidelines for addressing the major issues that arise in the CFD simulation of hydraulic components. In particular, the approach to modelling the turbulent flows has been investigated and the results that can be obtained by adopting different numerical models have been compared. Furthermore, the influence of the boundary layer resolution as well as the cell dimension on the predictive capabilities has been addressed. Additionally, the importance of accounting for cavitation and aeration in the numerical modelling has been evidenced and the effects on the results' accuracy have been remarked. Finally, the steady state approach and the fully transient simulation have been confronted in terms of predictive capabilities of the behaviour of internal flow field of a hydraulic component, complexity and required time for the case set up as well as the computational effort and simulation duration. The results that can be obtained by means of the multidimensional numerical analysis of hydraulic systems have been discussed in terms of pressure and velocity distribution and recirculating regions within the components and of overall performance parameters, such as the discharge coefficient, the flow acceleration angle and the flow forces. In the chapter, the methodology for the multidimensional design of hydraulic systems has been applied to the analysis of a closed centre electro-hydraulic load-sensing proportional control valve, usually adopted in multi-slice blocks to control parallel actuations of industrial, agricultural and earthmoving machines. Examples of results that can be obtained by the numerical simulation have been provided and discussed in the terms of component performance and influence on the

system operations. Furthermore, the same approach has been employed in the investigation of a low pressure, common rail, multi-fuel injection system. The behaviour of the injection system and in particular of the injector has been addressed under different operating conditions, and its performance has been also evaluated when extending the working range to higher pressure and to different fuel mixtures. The multidimensional CFD approach demonstrated to be a valuable tool in the design of hydraulic components and systems, since it provides reliable and accurate results on the flow behaviour that can help the designer understand their operations and improve the performance.

8. References

Barman, P. (2005). Computational fluid dynamic (CFD) analysis to optimize the pump suction line configuration of a hydraulic control system, *SAE 2005-01-3633* , ISSN 0148 – 7191

Beaudoin, M. & Jasak, H. . (2008). Development of a Generalized Grid Interface for Turbomachinery simulations with OpenFOAM. *Proceeding of the 2008 2nd Open Source CFD International Conference*, Berlin, Germany, December 4-5, 2008

De Villiers, E., Gosman, D. & Weller, H. (2004). Detailed Investigation of Diesel Spray Atomisation Using Quasi-Direct CFD Simulation, *Proceedings of the JSME 2004 6th International Symposium on Diagnostics and Modeling of Combustion in Internal Combustion Engines*, Vol.2004, No.6, pp. 295-302, Yokohama, Japan, August 2-5, 2004

Launder, B.E. & Sharma, B.I. (1974) Application of the Energy Dissipation Model of Turbulence to the Calculation of Flow Near a Spinning Disk, *Letters in Heat and Mass Transfer*, Vol.1, No.2, pp. 131-137, ISSN 0735-1933

Menter, F.R. (1993). Zonal Two Equation k-ω Turbulence Models for Aerodynamic Flows, *Proceedings of AIAA 1993 23rd Fluid Dynamics, Plasmadynamics, and Lasers Conference*, pp. 1-21, ISSN 0001-1452, Orlando, Florida, USA, July 6-9, 1993

Menter, F.R. (1994) Two-Equation Eddy-Viscosity Turbulence Models for Engineering Applications, *AIAA Journal*, Vol.32, No.8, pp. 1598-1605, ISSN 0001-1452

Ohm, T. R., Senser, D. W. & Lefebvre, H. (1991). Geometrical effects on discharge coefficients for plain-orifice atomizers, *Atomization and Sprays*, Vol.1, No.2, pp. 137-153, ISSN: 1044-5110

OpenCFD (2010). *OpenFOAM 1.7.1*, August 26 2010, Available from: http://www.openfoam.co.uk

OpenFOAM®-Extend Project (2010). *OpenFOAM 1.6-ext*, November 26 2010, Available from: http://www.extend-project.de

Oshima S. & Ichikawa T (1985). Cavitation Phenomena and Performance of Oil Hydraulic

Poppet Valve, *Bulletin of JSME*, Vol.28 No.244, pp. 2264-2271, ISSN: 1881-1426

Oshima S. & Ichikawa T. (1986). Cavitation Phenomena and Performance of Oil Hydraulic Poppet Valve, *Bulletin of JSME*, Vol.29 No.251, pp. 1427-1433, ISSN: 1881-1426

Oshima, S., Leino, T., Linjama, M., Koskinen, K. T. & Vilenius, M. J. (2001). Effect of Caviation in Water Hydraulic Poppet Valves, *International Journal of Fluid Power*, Vol.2, No.3, pp 5 -13, ISSN 1439-9776

Pao, R. H. F. (1967) *Fluid Mechanics*, John Wiley & Sons, Inc, Publishers. ISBN 61-11499, New York, USA

Payri, R., Margot, X. & Salvador, F. (2002). A NumericalStudy of the Influence of Diesel Nozzle Geometry on the Inner Cavitating Flow, *SAE 2002-01-0215*, ISSN 0148 – 7191

Ramamurthi, K. & Nandakumar, K. (1999). Characteristics of flow through small sharp-edged cylindrical orifices, *Flow Measurement and Instrumentation*, Vol.10, No.3, pp. 133–143, ISSN 0955-5986

Weiss, R.F. (1970). The solubility of nitrogen, oxygen and argon in water and seawater, *Deep Sea Research and Oceanographic Abstracts*, Vol.17, No.4, pp. 721-735, ISSN 0967-0637

Wilcox, D.C. (1988) Reassessment of the Scale-Determining Equation for Advanced Turbulence Models, *AIAA Journal*, Vol.26, No.11, pp. 1299-1310, ISSN 0001-1452

Yadigaroglu, G. & Lahey, R. T. Jr. (1976). On the Various Forms of the Conservation Equations in two Phase Flow, *International Journal of Multiphase Flow*, Vol. 2, No. 5-6, pp. 477-494, ISSN 0301-9322

Yang, R. (2002). Simulations of Oil Flow and Flow-Induced Forces Inside Hydraulic Valves, *SAE 2002-01-1376* , ISSN 0148 – 7191

Yang, R. (2005). Predicting Hydraulic Valve Pressure Drop Using CFD, *SAE 2005-01-3635*, ISSN 0148 – 7191

Zarotti, G. (1998). *Fluidi Oleodinamici – nozioni e lineamenti introduttivi*, Vol.2. CEMOTER-CNR

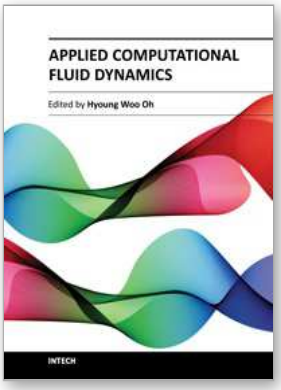

Applied Computational Fluid Dynamics

Edited by Prof. Hyoung Woo Oh

ISBN 978-953-51-0271-7
Hard cover, 344 pages
Publisher InTech
Published online 14, March, 2012
Published in print edition March, 2012

This book is served as a reference text to meet the needs of advanced scientists and research engineers who seek for their own computational fluid dynamics (CFD) skills to solve a variety of fluid flow problems. Key Features: - Flow Modeling in Sedimentation Tank, - Greenhouse Environment, - Hypersonic Aerodynamics, - Cooling Systems Design, - Photochemical Reaction Engineering, - Atmospheric Reentry Problem, - Fluid-Structure Interaction (FSI), - Atomization, - Hydraulic Component Design, - Air Conditioning System, - Industrial Applications of CFD

INTECH
open science | open minds

InTech Europe
University Campus STeP Ri
Slavka Krautzeka 83/A
51000 Rijeka, Croatia
Phone: +385 (51) 770 447
Fax: +385 (51) 686 166
www.intechopen.com

InTech China
Unit 405, Office Block, Hotel Equatorial Shanghai
No.65, Yan An Road (West), Shanghai, 200040, China
中国上海市延安西路65号上海国际贵都大饭店办公楼405单元
Phone: +86-21-62489820
Fax: +86-21-62489821